Bulletin of the Seismological Society of America, Vol. 105, No. 1, pp. 330–340, February 2015, doi: 10.1785/0120140151

The 8 October 2011 Earthquake at El Hierro (M_w 4.0): Focal Mechanisms of the Mainshock and Its Foreshocks

by Carmen del Fresno, Itahiza Domínguez Cerdeña, Simone Cesca,* and Elisa Buforn†

Abstract We have studied the focal mechanism of an M_w 4.0 earthquake that occurred on 8 October 2011 in the southwest of El Hierro (Canary Islands), the largest shock of the swarm that preceded the submarine eruption of El Hierro 2011–2012. The joint focal mechanism solution of 34 foreshocks has also been obtained. The results for the mainshock are consistent with a pure double-couple mechanism of a strike-slip motion with a reverse component and a focal depth of 12–13 km. The stress pattern obtained from the focal mechanism indicates horizontal compression in a north-northwest–south-southeast direction, parallel to the southern ridge of the island, and a quasi-horizontal extension in an east–west direction. Similar stress pattern is derived from the joint solution of the foreshocks. The occurrence of this family of earthquakes at the moment of the maximum strain rate of the pre-eruptive swarm suggests that their rupture process is related to tectonic stress, which led to the eruption only two days later, 5 km away from the mainshock epicenter.

Introduction

Seismic sources of crustal tectonic earthquakes are related to local stress patterns and an analysis of their focal mechanisms can help to understand the physical process of magma migration in active volcanic islands (Roman and Cashman, 2006; Umakoshi *et al.*, 2011; Silva *et al.*, 2012). However, scarce focal mechanism data is a common characteristic in the whole Canarian archipelago. The first fault-plane solution was performed by Mezcua *et al.* (1992), who estimated the fault-plane orientation of a 5.2 magnitude earthquake between the islands of Gran Canaria and Tenerife using *P*-wave first-motion data. Since then, no other source studies have been published for this region. In addition, the two automatic solutions in the regional moment tensor (MT) catalog of the Instituto Geográfico Nacional (IGN) corresponding to this area are poorly resolved due to the low-azimuthal coverage on the regional network.

The 2011–2012 eruption of El Hierro is the first eruption of the twenty-first century in the Canary Islands. During the previous century, three eruptions took place in the archipelago: one in Tenerife (1909) and two in La Palma (1971, 1949) (Fig. 1) (e.g., Carracedo *et al.*, 2001, 2007). The 2011–2012 eruption was the first historical eruption in El Hierro and the first documented submarine eruption in the whole archipelago. The eruption was preceded by a three-month dense seismic swarm (Carracedo *et al.*, 2012; Ibáñez *et al.*, 2012; López *et al.*, 2012; Martí *et al.*, 2013). The anomalous activity started on 19 July 2011 beneath the center of the island, at a depth of ∼10–15 km (Domínguez Cerdeña *et al.*, 2014). Two weeks later, the seismicity migrated ∼2 km northward. During the first week of September, a gradual migration of hypocenters toward the south coast of the island was accompanied by a gradual increase in magnitudes. A drastic increase in seismicity rates and magnitudes occurred during the last week of September and the first days of October, with epicenters mostly located offshore, southwest of the island. On 8 October 2011 20:34:48 UTC, an M_L 4.3 occurred. This was the largest earthquake of the pre-eruptive swarm and will be the object of our study (Fig. 1). According to the IGN database, this shock was located 1 km offshore from the southwest coast of El Hierro at a depth of 12 km. In terms of intensity, the earthquake was clearly felt in the entire island territory and the maximum intensity value of V, per the European Macroseismic Scale 1998 (EMS-98), was reached in La Restinga on the southern edge of the island. This earthquake played a significant role in the 2011 reactivation, as the pattern of the volcanic unrest changed considerably in the following hours: a clear change in the trend of the superficial deformation was observed, a swarm of shallow seismicity (depths in the 1–6 km range) started offshore, south of the island, and finally, 32 hours after the earthquake occurred, the eruption began less than 5 km from its epicenter (López *et al.*, 2012; Martí *et al.*, 2013).

To study the focal mechanism of this earthquake, a point-source MT inversion was performed by fitting the amplitude spectra at regional and local distances. In an additional step,

*Also at Institut für Erd- und Umweltwissenschaften, University of Potsdam, Karl-Liebknecht-Str. 24-25, 14476 Potsdam-Golm, Germany.

†Also at Instituto de Geociencias (IGEO), UCM-CSIC, Madrid, Spain.

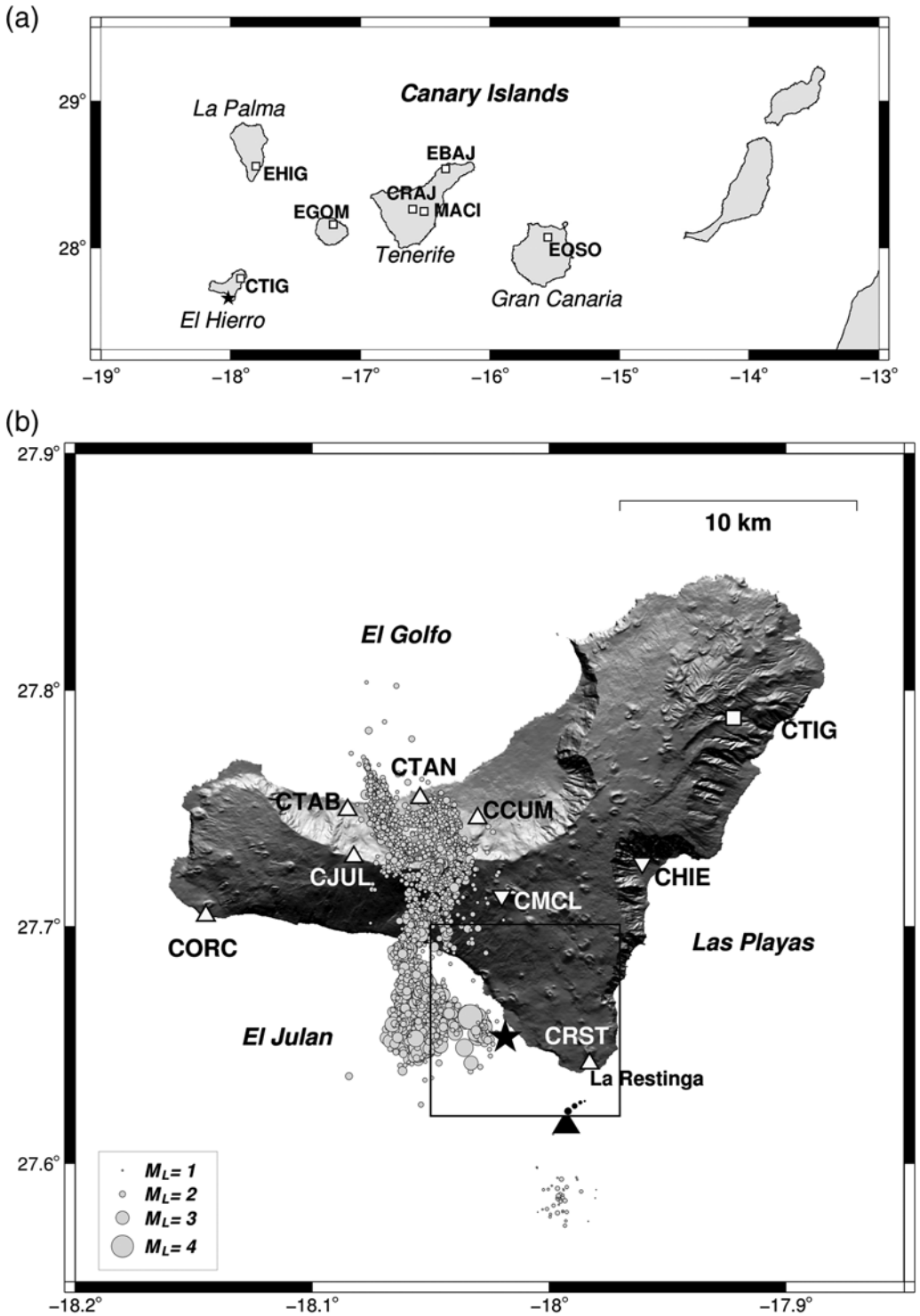

Figure 1. (a) The Canarian archipelago with El Hierro highlighted and the distribution of the broadband seismic stations of the regional network (Instituto Geográfico Nacional [IGN]) used in this work. (b) Distribution of the epicenters in El Hierro from 17 July 2011 to 10 October 2011 according to the relocation of Domínguez Cerdeña *et al.* (2014). Black star indicates the epicenter of the M_L 4.3 earthquake (IGN database). The distribution of the seismic network in El Hierro: the 3C broadband seismometer (square), the 3C short-period sensor (triangles), and the vertical short-period seismometers (inverted triangles). The area marked with a dark square corresponds to Figure 5b.

we searched for earthquakes with similar waveform data as the mainshock, exploited the waveform similarities to improve their relative location, and obtained an estimate of the joint focal mechanism solution. In the following, we discuss the results of this work in the context of the whole unrest sequence and the seismotectonics of the region.

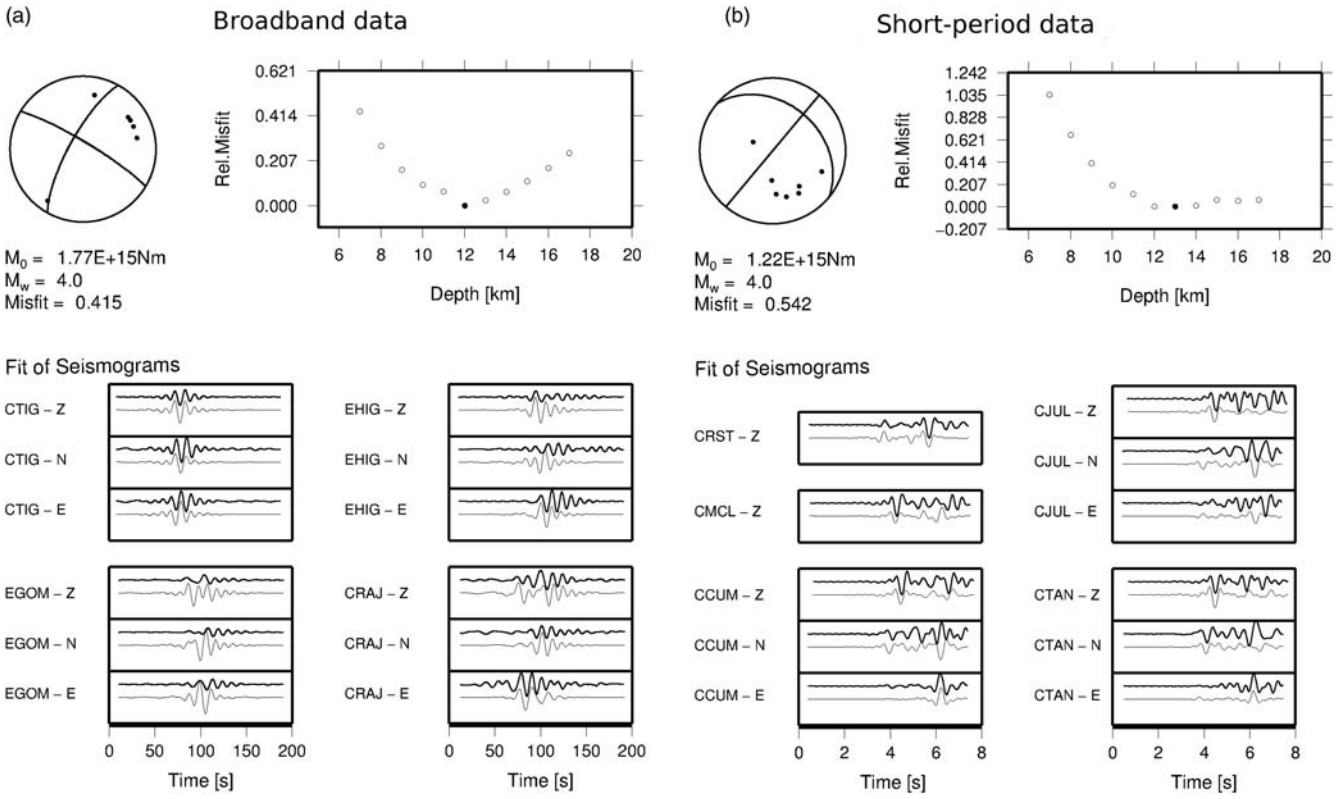

Figure 2. Results of the point-source double-couple inversion and examples of the fit of seismograms of the closest stations corresponding to (a) regional distances using broadband data and (b) local distances using short-period data.

Focal Mechanism of the Mainshock

As a first approach, a kinematic point-source inversion was performed assuming a double-couple (DC) model. We retrieved the strike, dip, rake, scalar moment, and centroid depth of the main earthquake using an algorithm based on the Kiwi tools (Cesca *et al.*, 2010; Heimann, 2011). We chose a frequency-domain inversion approach, fitting the amplitude spectra, rather than the time trace, as this method is less sensitive to a precise trace alignment and to phase shifting owing to mismodeling of the crustal structure (Romanowicz, 1982; Cesca *et al.*, 2006). This approach is helpful for more precise source depth estimates but has a disadvantage: compression and dilatation quadrants of the focal sphere cannot be distinguished. For this reason, polarity data were considered in the last inversion step to resolve this ambiguity. Given the nonlinearity of the inversion and the possible nonuniqueness of the solutions, each inversion was run several times, using a set of different starting configurations (see also Cesca *et al.*, 2013). A Green's functions database was previously built based on the Dañobeitia (1980) crustal velocity model, which was used for the absolute locations in the IGN catalog and for previous seismicity studies of the El Hierro region (Domínguez Cerdeña *et al.*, 2014). An AK135 model was considered for the upper mantle.

We performed two independent inversions using different datasets, due to critical differences in terms of instrumentation: the first inversion relies on broadband data from the permanent network of the whole Canarian archipelago (Fig. 1a), whereas the second one takes into account the short-period instruments of the temporary network of El Hierro (Fig. 1b). For the regional inversion with the broadband data, we used data from seven stations from the permanent regional IGN network in the archipelago, using a total of 19 traces (the horizontal components of EBAJ station were not taken into account due to the low signal-to-noise ratio). The epicentral distances vary from 20 to 250 km, and only the closest station (CTIG) is installed on the island of El Hierro. We considered full waveform displacement data, with a window length of 180 s. The data were filtered using a band-pass filter between 0.033 and 0.1 Hz and a sampling rate of five samples per second (samples/s). The results of the inversion showed an almost pure strike-slip mechanism (Fig. 2a) with fault planes oriented at 208° N and 300° N. The centroid is found at a depth of 12 km, with a scalar moment of M_0 1.8×10^{15} N·m (M_w 4.0). For the local inversion with short-period data, we used 15 traces from seven stations located on El Hierro, which are also operated by IGN. The epicentral distances of the local network range from 0 to 15 km. A window length of 7 s was selected, and the horizontal components were considered half the weight of the vertical ones. A band-pass filter between 1 and 3 Hz and a sampling rate of 50 samples/s were used. The results of the inversion showed an oblique (thrust to strike slip) focal mechanism (Fig. 2b). One plane is almost vertical, with an azimuth of

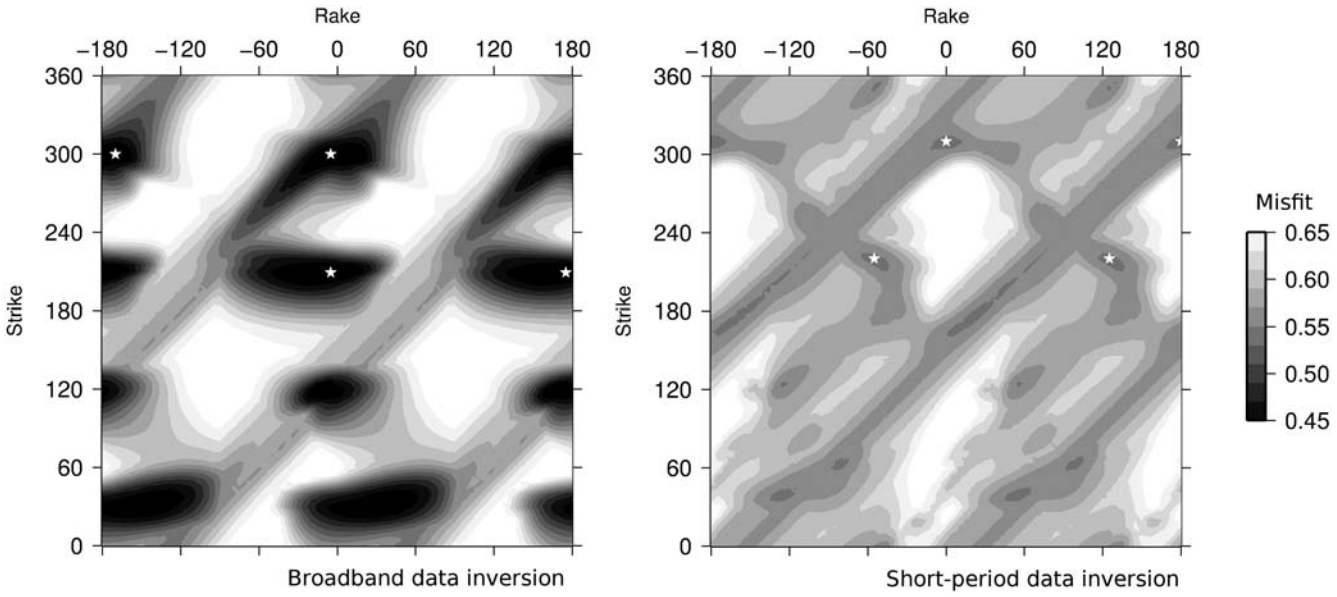

Figure 3. Distribution of the misfit values obtained in the broadband and short-period data inversions on a strike-rake diagram. The stars indicate the four fault-plane solutions with minimum misfit for each inversion, which corresponds to the solutions of Figure 2.

218°; the second plane has a low-angle dip of 38° and a northwest–southeast strike direction. The centroid corresponds to a depth of 12 km, and the scalar moment obtained is $M_0 = 1.2 \times 10^{15}$ N·m (M_w 4.0).

The results of both inversions are consistent in terms of magnitude and source depth but partially differ in terms of the resolved focal mechanism. These results may be affected by the strong station asymmetry and the azimuthal gap. To check their quality and uncertainties, we performed a detailed grid search in the model space of strike, dip, and slip. As an example of this analysis, Figure 3 compares the misfit distribution of both inversions projected on a strike-rake diagram. It is shown in the figure that the regional inversion presents lower-misfit values, which are desirable in terms of stability for inversion methodologies. However, wider minimum areas were found, underlying a lower resolution, a finding that is possibly due to the lower-azimuthal coverage. The results of the local inversion yielded narrower and better constrained minimum misfit regions, when projected on a strike-rake diagram, but the misfit values were slightly larger than the regional inversion. This fact can be related to unmodeled lateral heterogeneities in the crustal structure, which can considerably affect the higher-frequency waveforms recorded at local distances (Cesca *et al.*, 2008).

To jointly interpret both inversion results, we calculated the average misfit value for each strike-dip-slip configuration (Fig. 4). This process enhances the common minimum misfit regions of the solution space, leading to a more constrained solution. This, in turn, joins the information and higher-azimuth coverage of high frequencies at local distances with the stability of the lower frequencies of broadband sensors at regional distances. The final result is shown in Figure 4 and consists of nearly a strike-slip motion with a reverse component. The four fault-plane solutions were strike 295°, dip 40° with rakes 165° and −15°, and strike 37°, dip 80° with rakes 51° and −129°. The minimum misfit corresponds to a value of $M_0 = 1.3 \times 10^{15}$ N·m (M_w 4.0).

Finally, we analyzed the polarity data of the *P* and *SH* waves to determine the compression and dilatation quadrants. The FOCMEC package (Snoke *et al.*, 1984) was used to summarize all acceptable solutions that fit the observed polarities. To obtain reliable solutions, we only included clear impulsive polarity data. We considered the same velocity model as in the inversion. We did not allow any polarity error in the solutions due to the limited number of observations available (15 *P* and 6 *SH*). Figure 4 shows the polarity data along with the set of solutions that satisfy them and illustrates the compatibility among the polarities and amplitude spectra inversion solutions.

We also tested the inversion of regional and local data considering a full MT point-source model. Although some non-DC components are found, the new misfit values do not considerably improve with respect to those obtained for the best DC models. Moreover, full MT solutions have a worse fit in observed first-motion polarities.

Cluster Identification and Relative Location

In this section, we search for the family of earthquakes that have high-correlation factors with the mainshock, with the aim of identifying those earthquakes with similar focal mechanisms and hypocenter locations as the largest one. The analysis of the resulting family can provide interesting details of the source process. A relative location of the family can contribute information on the orientation of the source-

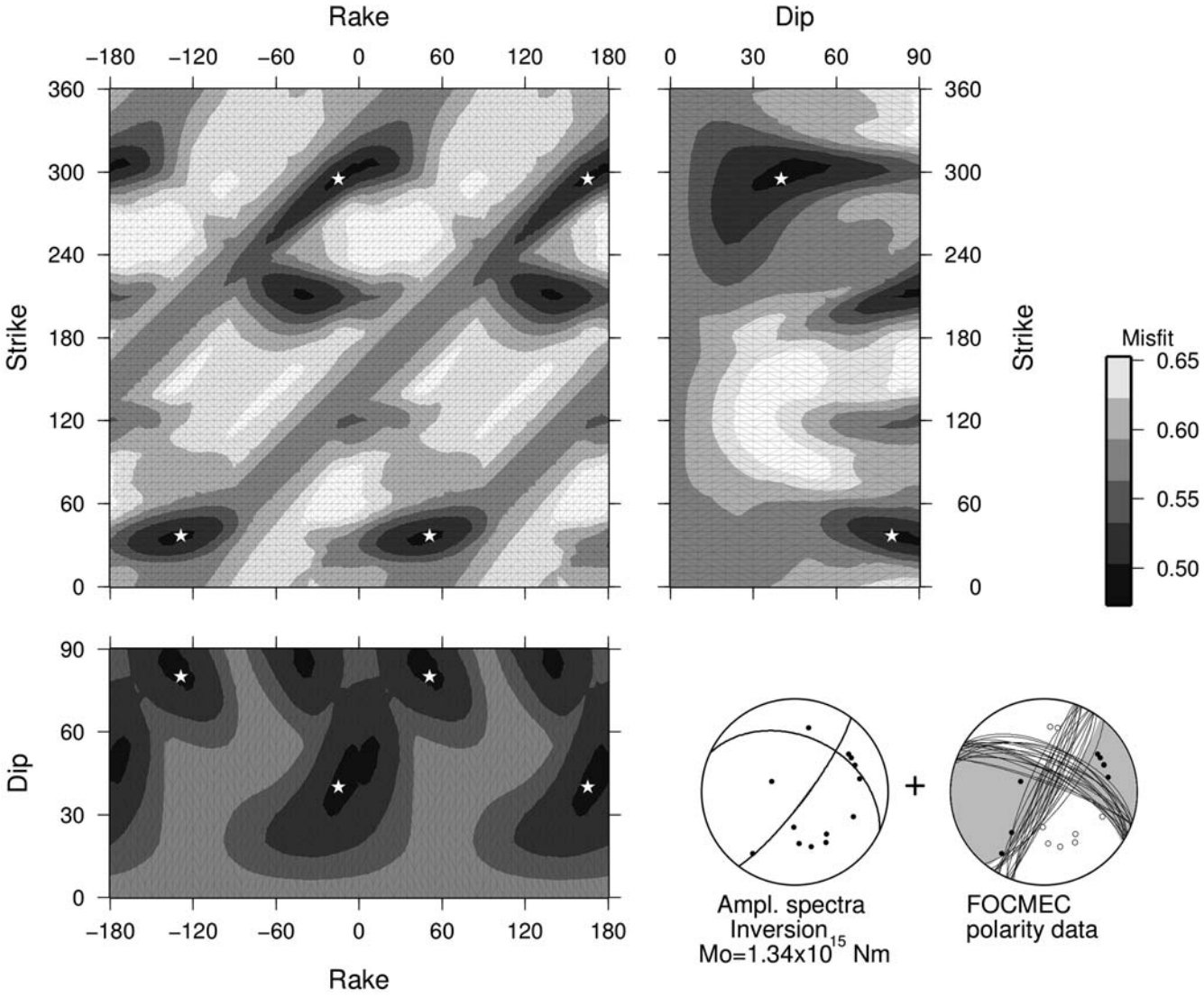

Figure 4. Results of the inversion combining the local and regional results over the strike-dip-rake space of solutions. The stars correspond to the fault-plane values that minimize the amplitude spectra (four possible combinations). On the bottom center of the obtained focal mechanism, the dots on the focal sphere represent stations considered in the inversion. On the bottom right, the FOCMEC solution of *P* and *SH* polarities, with the open circles indicating dilatations and the black circles corresponding to compressions.

rupture process and will also allow us to estimate the joint fault-plane solution of these earthquakes.

The method used to identify the family of events is equivalent to that of Domínguez Cerdeña *et al.* (2011) and can be briefly described as follows: we cross correlated the mainshock waveforms with those earthquakes located in the pre-eruptive swarm, with local magnitudes greater than 1.5 in the IGN catalog, for a total of ∼3600 earthquakes. We chose a threshold level of 0.7 for the correlation factor. The analysis was performed using three-component data from five stations (CORC, CTAB, CTAN, CCUM, and CTIG; see Fig. 1), ensuring the waveform similarities at different azimuths to infer a similar radiation pattern. A window length of 8 s was used for the correlation, starting 2 s before the *P* arrival. As the cross-correlation analysis is sensitive to the frequency content of the waveforms, which depends on the size of the considered earthquake, we evaluated the cross correlation after filtering the velocity records in the frequency band of 1–4 Hz, which corresponds to the flat part of the spectrum of the main earthquake. Testing a broader range of band-pass filters runs the risk of clustering only the largest events, thus missing the information from the low-magnitude events, which are also important for the interpretation of the results.

The cluster analysis resulted in a family of 34 foreshocks. Figure 5a shows an example of three-component raw velocity seismograms of some of the family earthquakes recorded at station CORC (bottom waveforms correspond to the mainshock). A comparison of these waveforms points out obvious common features within the family supporting a similar hypocentral location and radiation pattern, despite the different frequency content, which is a consequence of

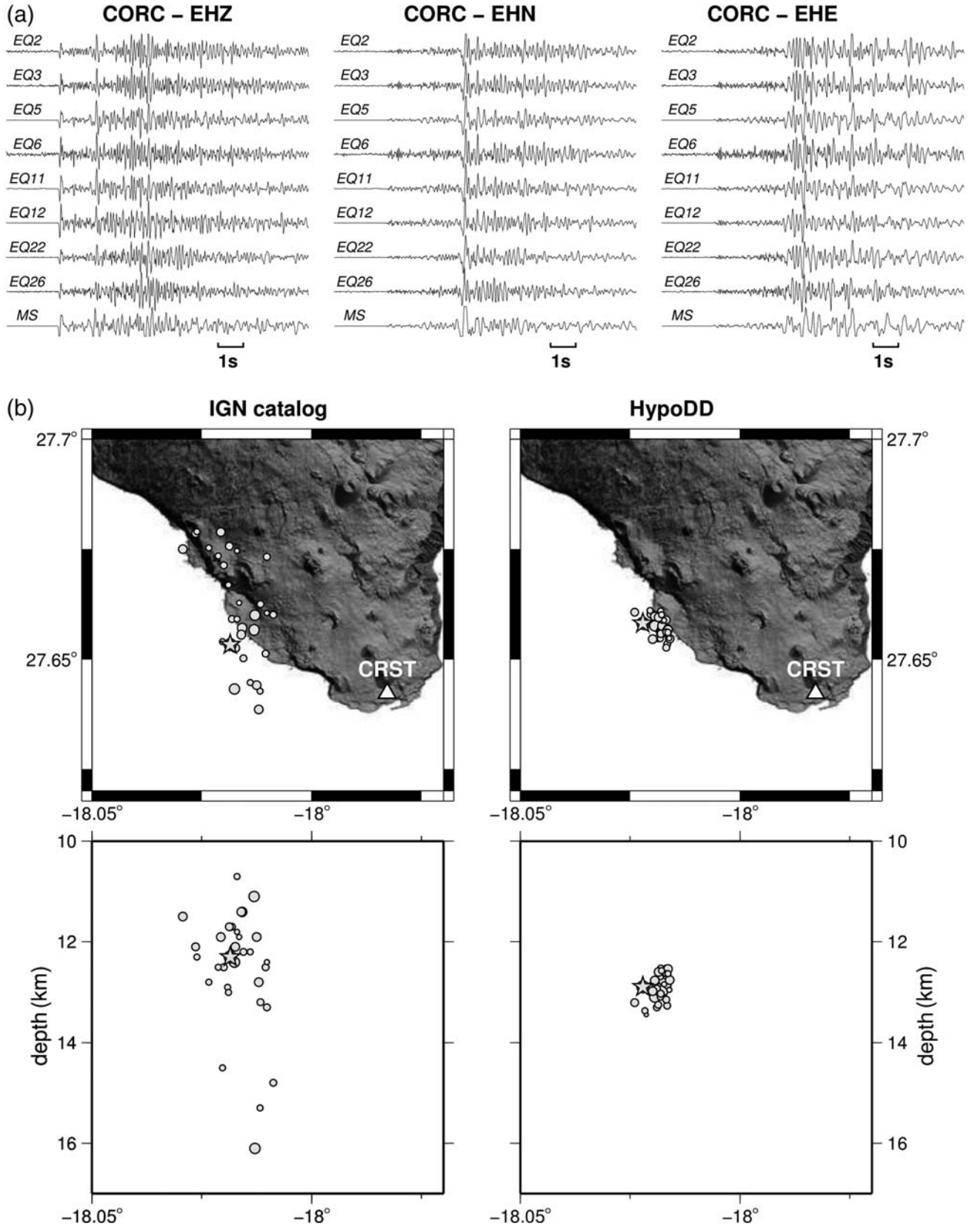

Figure 5. (a) Velocity waveforms of some earthquakes of the mainshock family, recorded at the CORC station in the vertical component. The numbers of each trace correspond to the event number in Table 1. (b) An epicentral location comparison between the original catalog hypocenters (top left) and the results obtained by hypoDD (top right), and the corresponding vertical cross sections in east–west directions (bottom right and left, respectively). The vertical axes on the cross sections have been cropped from a depth of 10–17 km to keep the same vertical and horizontal scale.

different earthquake sizes. The IGN local magnitudes of the retrieved family vary from M_L 1.6 to 3.8. All events occurred in the last 23 hours preceding the mainshock and the seismicity rate for this family decreased with time, with most earthquakes occurring in the first eight hours. Figure 5b (left) shows the epicenters of the resulting family according to the IGN catalog (top) and their hypocentral locations in a vertical east–west cross section (bottom). We observe a scattered distribution around the mainshock with no clear alignment in any direction. The location errors from these catalog locations have a mean value of 2 km in horizontal sense and 3 km in depth (90% confidence). The higher uncertainties correspond to smaller events that imply a scarce number of stations used in the location process.

We performed a relative location of the family using the hypoDD algorithm (Waldhauser and Ellsworth, 2000). We used travel-time differences from *P* and *S* waves manually picked along with travel-time differences computed by cross correlation for all possible combinations of the earthquakes of the family. Data from every station of El Hierro were used considering time windows of 2 and 3 s length for *P*- and *S*-wave correlations, respectively. We considered the same velocity model as in the mainshock inversion. The results of the hypocenter relocations show a much tighter spatial clustering (Fig. 5b, right) than the original locations in the IGN catalog. All of the earthquakes in the family are located within a $1 \times 1 \times 1$ km region, showing that all events arise from a small, unmoving, repeating source. Their epicenters are aligned along a northwest–southeast direction along the coastline, which corresponds to the striking of one of the resolved fault planes. The clustering is also evident in their hypocentral depths, which vary from 12.5 to 13.4 km. The mainshock hypocenter is located 500 m northwest from the original absolute location in the northwestern edge of the cluster at a depth of 12.9 km.

To assess the uncertainties of the relative relocated hypocenters, we applied the statistical resampling bootstrap method (Efron, 1982) and the same criterion as in Domínguez Cerdeña *et al.* (2014). Mean values of 800 m were obtained for the maximum semiellipse axes (S_{max}) and 300 m for the minimum semiellipse axes (S_{min}). Error ellipses oriented in a north-northwest–south-southeast direction. The mean vertical error obtained was 1 km.

Magnitude Determination and Joint Source Mechanism for the Relocated Cluster

To homogenize the magnitude of all the family earthquakes, we estimated their scalar seismic moments (M_0) and moment magnitudes (M_w) from the spectral analysis of *P* waves (Table 1). The number of stations used for each earthquake varies from 7 to 12 stations. An $M_0 = (1.2 \pm 0.9) \times 10^{15}$ N·m was obtained for the mainshock, which corresponds to an M_w 4.0. For the rest of the cluster, M_0 values range from 3.0×10^{12} N·m to 2.3×10^{14} N·m ($2.3 \leq M_w \leq 3.5$). Although the largest earthquake is the last one in the sequence, there is no clear temporal evolution of the earthquakes' sizes.

The joint fault-plane solution for the 34 selected earthquakes was estimated using the MECSTA code (Udías and Buforn, 1988). This algorithm estimates the maximum likelihood function of observed and theoretical data of a point-source DC model and calculates the strike, dip, and rake of both nodal planes, *T* and *P* axes orientation, and the statistical error of each parameter. The number of *P*-wave polarity per earthquake varies between a minimum value of six and a maximum of 11 stations with a total of 307 observations. The results corroborate that all of the earthquakes considered belong to the same focal mechanism, as was expected by their similar waveforms and the high cross-correlation factors with the mainshock. A high score of 0.91 and a vertical strike-slip mechanism were retrieved (Fig. 6a). Fault-plane orientations are a first plane with strike $= 291° \pm 7°$ and dip $= 71° \pm 28°$, and the second plane with strike $= 195° \pm 7°$ and dip $= 74° \pm 11°$.

Discussion and Conclusions

The results obtained in this work reveal important features of the source mechanism of the M_w 4.0 earthquake that occurred on 8 October 2011 and its foreshocks.

A hypocenter depth of 12–13 km is obtained from the mainshock inversion. The relative locations of the whole family of earthquakes studied here show a tight cluster of hypocenters at similar depths with no apparent migration. These values correspond to the bottom of the crust in this region (Watts, 1994; Ranero and Torne, 1995) and are compatible with locations of magma pockets below El Hierro computed by Stroncik *et al.* (2009). Moreover, texture, petrography, and geochemical compositions of the products emitted during the early phases of the 2011 eruption also indicate a fast ascent from a reservoir located 12–14 km deep (Meletlidis *et al.*, 2012). The epicenters are located in an area that has been interpreted as the feeding system of the southern ridge, as it presents the highest magnetizations of the region at the present time (Blanco-Montenegro *et al.*, 2008).

The source mechanism obtained from the mainshock inversion indicates a strike-slip motion with a reverse component and fault planes oriented on northeast-southwest and west-northwest–east-southeast directions (Fig. 6b). It is difficult to decide whether there is a preferred fault plane on the joint solution, but the alignment of the foreshock epicenters induce us to prefer the west-northwest–east-southeast oriented plane as the rupture plane. The M_0 obtained from the inversion and spectral analysis is similar and corresponds to an M_w 4.0.

It has been shown that certain processes in volcanic regions, such as magmatic and hydrothermal fluid migration, may be accompanied by earthquakes with significant non-DC components (Shuler *et al.*, 2013). However, results obtained in this work indicate the seismological observations both at local and regional distances can be well reproduced by a pure DC model for a shear failure on a planar fault. The high

Table 1
Cluster Events Relocated by the Double-Difference Method

Date (yyyy/mm/dd)	Time (hh:mm:ss)	Latitude (°)	Longitude (°)	Depth (km)	Nsta*	M_0 (N·m)*	M_w*	Corr*	Ref*
2011/10/07	22:14:08	27.657	−18.021	13.4	9	$(3 \pm 2) \times 10^{12}$	2.3 ± 0.1	0.70	EQ1
2011/10/07	22:20:48	27.657	−18.019	13.3	9	$(7 \pm 6) \times 10^{12}$	2.5 ± 0.2	0.73	EQ2
2011/10/07	22:24:21	27.655	−18.019	13.3	9	$(6 \pm 3) \times 10^{12}$	2.5 ± 0.1	0.81	EQ3
2011/10/07	22:25:56	27.658	−18.019	13.1	9	$(2 \pm 1) \times 10^{14}$	3.5 ± 0.2	0.92	EQ4
2011/10/07	22:27:45	27.656	−18.018	13.0	9	$(2 \pm 1) \times 10^{14}$	3.5 ± 0.2	0.85	EQ5
2011/10/07	22:30:05	27.655	−18.018	13.1	9	$(5 \pm 3) \times 10^{12}$	2.4 ± 0.2	0.76	EQ6
2011/10/07	22:32:50	27.657	−18.022	13.4	9	$(1.1 \pm 0.9) \times 10^{13}$	2.6 ± 0.2	0.71	EQ7
2011/10/07	22:35:13	27.657	−18.018	13.0	9	$(5 \pm 4) \times 10^{12}$	2.4 ± 0.2	0.73	EQ8
2011/10/07	22:41:33	27.657	−18.018	12.8	8	$(7 \pm 3) \times 10^{12}$	2.5 ± 0.1	0.70	EQ9
2011/10/07	22:52:25	27.660	−18.020	12.9	9	$(6 \pm 3) \times 10^{13}$	3.1 ± 0.2	0.92	EQ10
2011/10/07	22:52:58	27.656	−18.018	13.0	9	$(1.2 \pm 0.7) \times 10^{14}$	3.3 ± 0.2	0.83	EQ11
2011/10/07	22:56:15	27.658	−18.018	12.8	9	$(6 \pm 4) \times 10^{13}$	3.1 ± 0.2	0.85	EQ12
2011/10/07	23:01:06	27.660	−18.019	12.9	9	$(1.4 \pm 0.9) \times 10^{13}$	2.7 ± 0.2	0.86	EQ13
2011/10/07	23:04:59	27.661	−18.021	12.9	8	$(4 \pm 3) \times 10^{12}$	2.3 ± 0.2	0.74	EQ14
2011/10/07	23:12:08	27.659	−18.018	12.8	8	$(6 \pm 3) \times 10^{12}$	2.5 ± 0.1	0.78	EQ15
2011/10/07	23:12:30	27.657	−18.017	12.9	8	$(1.1 \pm 0.6) \times 10^{13}$	2.6 ± 0.1	0.75	EQ16
2011/10/07	23:17:04	27.659	−18.018	12.7	9	$(1.0 \pm 0.7) \times 10^{13}$	2.6 ± 0.2	0.85	EQ17
2011/10/07	23:30:35	27.661	−18.024	13.2	10	$(3 \pm 2) \times 10^{13}$	2.9 ± 0.2	0.84	EQ18
2011/10/07	23:37:46	27.656	−18.018	13.0	10	$(1.3 \pm 0.8) \times 10^{13}$	2.7 ± 0.2	0.77	EQ19
2011/10/07	23:47:06	27.653	−18.017	13.3	9	$(3 \pm 2) \times 10^{13}$	2.9 ± 0.2	0.75	EQ20
2011/10/07	23:52:43	27.660	−18.019	12.8	9	$(5 \pm 4) \times 10^{13}$	3.1 ± 0.2	0.87	EQ21
2011/10/07	23:59:41	27.655	−18.020	13.0	9	$(7 \pm 4) \times 10^{13}$	3.2 ± 0.2	0.73	EQ22
2011/10/08	00:01:47	27.653	−18.017	13.2	9	$(2 \pm 1) \times 10^{13}$	2.8 ± 0.2	0.74	EQ23
2011/10/08	00:46:21	27.655	−18.016	12.8	10	$(3 \pm 2) \times 10^{13}$	2.9 ± 0.2	0.80	EQ24
2011/10/08	00:51:21	27.655	−18.016	13.0	8	$(5 \pm 3) \times 10^{12}$	2.4 ± 0.1	0.73	EQ25
2011/10/08	01:08:03	27.659	−18.017	12.5	10	$(2 \pm 1) \times 10^{13}$	2.8 ± 0.2	0.82	EQ26
2011/10/08	02:05:27	27.656	−18.017	12.6	8	$(5 \pm 3) \times 10^{12}$	2.4 ± 0.2	0.75	EQ27
2011/10/08	02:24:26	27.657	−18.016	12.5	9	$(3 \pm 2) \times 10^{13}$	2.9 ± 0.2	0.80	EQ28
2011/10/08	02:50:21	27.661	−18.018	12.5	9	$(8 \pm 5) \times 10^{12}$	2.5 ± 0.2	0.80	EQ29
2011/10/08	02:50:53	27.659	−18.019	12.6	9	$(5 \pm 3) \times 10^{13}$	3.1 ± 0.2	0.83	EQ30
2011/10/08	03:22:15	27.659	−18.017	12.8	7	$(3 \pm 2) \times 10^{12}$	2.3 ± 0.2	0.76	EQ31
2011/10/08	05:03:19	27.656	−18.017	12.6	8	$(3 \pm 2) \times 10^{12}$	2.3 ± 0.1	0.75	EQ32
2011/10/08	05:47:35	27.660	−18.018	12.6	8	$(4 \pm 2) \times 10^{12}$	2.3 ± 0.1	0.81	EQ33
2011/10/08	14:19:13	27.656	−18.016	12.6	9	$(4 \pm 2) \times 10^{12}$	2.3 ± 0.1	0.78	EQ34
2011/10/08	20:34:48	27.658	−18.022	12.9	12	$(1.2 \pm 0.9) \times 10^{15}$	4.0 ± 0.2	1.00	MS

*Seismic moment (M_0) and moment magnitude (M_w) were estimated from amplitude spectra analysis of *P* waves; Nsta, number of stations considered for the M_0 and M_w estimation; Corr, correlation factor to the largest earthquake; Ref, reference of each earthquake in this work.

agreement of the different approaches and the fit of spectra and waveforms in the inversion corroborate this fact. For this reason, a more complex model with non-DC components for this earthquake is discarded. The joint focal mechanism solution for the family of foreshocks (Fig. 6a) is also consistent with a pure DC mechanism, although the planes obtained are slightly steeper than those from the mainshock inversion.

A previous MT solution of the mainshock was calculated on near real time by the IGN as part of the regional MT catalog (Fig. 6c). The catalog was performed with automatic inversion of surface waves in the time domain (Rueda and Mezcua, 2005). The solution obtained for the M_w 4.0 earthquake was also a strike-slip motion but with a higher-reverse-fault component and a 12% compensated-linear-vector-dipole (CLVD) component. Despite a variation reduction higher than 75%, only one seismic station was used for the analysis, and the final solution does not satisfy some of the first-motion polarities recorded at the closest stations. Compared with our inversion results, the *P* axes are dipping to the northwest for the IGN solution, in contrast to the southeast dipping of our solution.

The focal mechanisms for both the mainshock and the joint foreshock solution correspond to a near horizontal maximum compression on a north-northwest–south-southeast direction, which matches well with the orientation obtained by Mezcua *et al.* (1992) for the 1989 earthquake, located more than 200 km northeast of the eruption. This orientation also agrees with the regional maximum compression in the archipelago, as obtained by neotectonic modeling in the region (Jiménez-Munt *et al.*, 2001) (Fig. 7). Although tension axes show slightly higher dispersion in the different estimates of this work and vary from east–west to east-southeast–east-northeast directions, they are consistent with the tectonic local stress of the Southern Ridge of El Hierro (Fig. 7). Two different models have been proposed to explain pressure axes parallel to principal stress orientation as the result of dike propagation in other volcanic regions: the first was proposed by Hill (1977), who located the earthquakes in volcanic environments

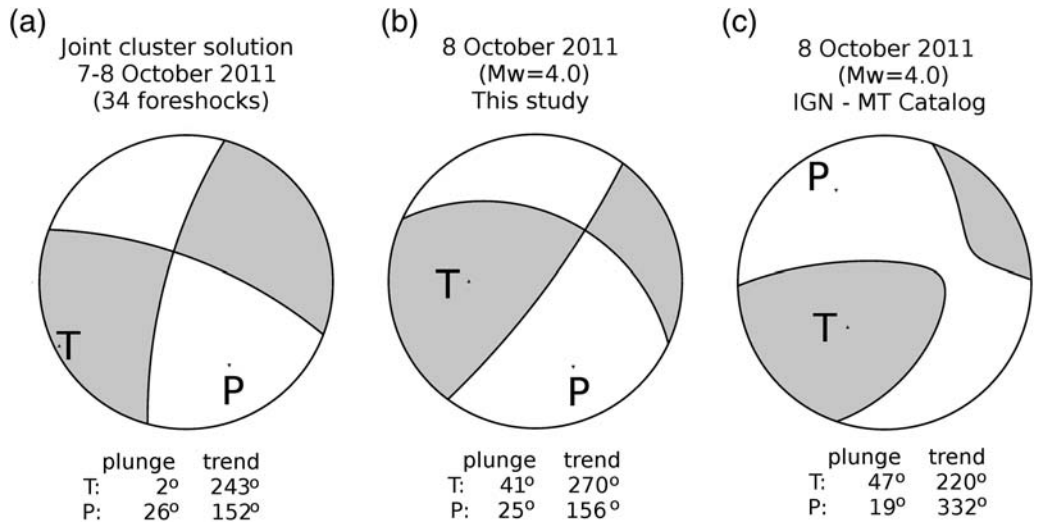

Figure 6. (a) A comparison of the results obtained for the joint fault-plane solution of the whole cluster, (b) the results of the M_w 4.0 obtained in this study through amplitude spectra inversion, and (c) the automatic moment tensor (MT) solution of the M_w 4.0 earthquake of the real-time MT catalog of the IGN.

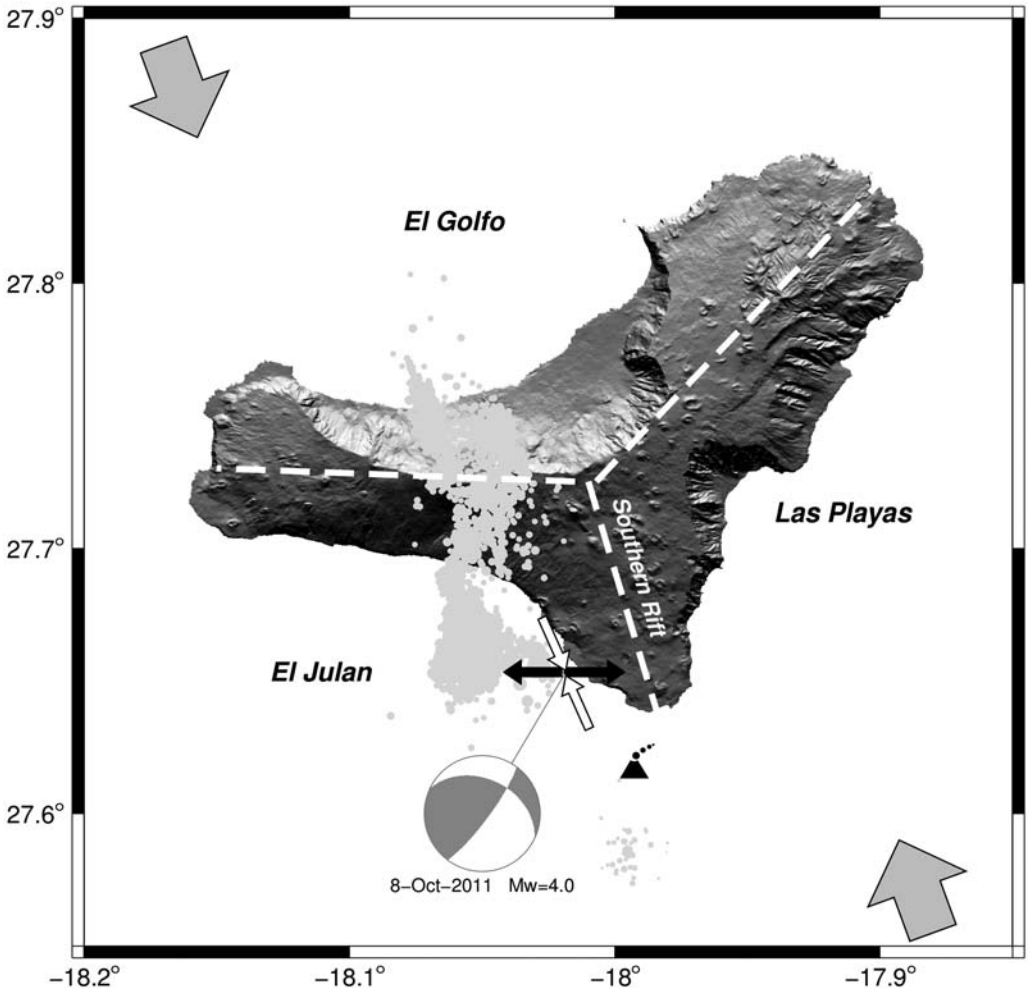

Figure 7. Map view of the pressure (white arrows) and tension axes (black arrows) of the 8 October 2011 M_w 4.0 earthquake, as well as the regional stress regime (thick arrows) and the three rift trends of El Hierro (white dashed line).

along shear planes connecting the edges of offset and inflating dikes; the second, proposed by Ukawa and Tsukahara (1996), suggests that the earthquakes occur on the tip of a propagating dike. Both models justify the strike-slip component of the mechanism of the earthquake in our work, as well as the lateral migration of the hypocenters of the overall 2011 activity. Furthermore, Roman and Cashman (2006) compared well-constrained case studies of numerous volcano-tectonic earthquake swarms and found that dike propagation appears to be recorded at volcanoes of basaltic composition located in strongly deviatoric local tectonic stress fields. All these conditions are satisfied at El Hierro.

Martí *et al.* (2013) considered the M_w 4.0 earthquake as the onset of the magma ascent to the surface. The results of our study indicate an important component of strike-slip fault as a consequence of the tectonic stress release and null isotropic component, which discards any volume changes in the source due to magma intrusion. Another interesting feature revealed in our study is that the main earthquake was the largest and latest part of a process that started the day before (7 October 2011, 22:14 UTC). This time coincides to when López *et al.* (2014) reports the beginning of the upward seismic hypocenter migration, the maximum release of seismic energy, and reaching the maximum strain rate of the pre-eruptive swarm and the first days of the eruption, and with gravity changes reported in Sainz-Maza Aparicio *et al.* (2014). Ibáñez *et al.* (2012) also observed a considerable decrease in b-values in that period compared to the previous weeks of the unrest.

In conclusion, despite the minimal amount of data, we can conclude that the focal mechanism of the M_w 4.0 earthquake (8 October 2011 22:34:48 UTC) correspond to a strike-slip motion with a reverse component and a focal depth of 12–13 km. This solution also agrees with the joint source solution for a family of 34 foreshocks, located very close to the mainshock. The stress pattern obtained from this focal mechanism indicates horizontal compression in a north-northwest–south-southeast direction, parallel to the southern ridge of El Hierro, and a quasi-horizontal extension in an east–west direction. The occurrence of this family of earthquakes at the moment of the maximum strain rate of the pre-eruptive swarm suggests that their rupture process is related to tectonic stress, which led to the submarine eruption two days later.

Data and Resources

The earthquake original catalog from the Instituto Geográfico Nacional (IGN) can be found in http://www.ign.es/ign/layoutIn/volcaFormularioCatalogo.do and the IGN moment tensor catalog database is accessible at http://www.ign.es/ign/layoutIn/sismoPrincipalTensorZonaAnio.do. Seismograms used in this study were collected by the National Seismic Network (IGN) and the Volcano Monitoring Group (IGN) and are currently not available to the public. Figures of this contribution have been plotted with Generic Mapping Tools version 4.2.1 (http://gmt.soest.hawaii.edu; Wessel and Smith, 1998) and MoPaD (Krieger and Heimann, 2012). Data analysis was completed using Pyrocko toolbox (http://emolch.github.io/pyrocko/) and the Seismic Analysis Code (http://www.iris.edu/dms/nodes/dmc/software/downloads/sac/; Goldstein and Snoke, 2005). All websites were last accessed in November 2014.

Acknowledgments

We would like to thank Associate Editor Allison Bent and two anonymous reviewers for their constructive suggestions. We also thank the National Seismic Network (Instituto Geográfico Nacional [IGN]) and the Volcano Monitoring Group (IGN) for the data, deployment, and maintenance of the seismic network on El Hierro. This work was funded by the Spanish Ministerio de Fomento, the Spanish Ministerio de Economía y Competitividad (Projects CGL2010-19803-C03-01 and CGL2013-45724-C3-R1), and project INNOCAMPUS Moncloa Campus of International Excellence. Simone Cesca is supported by the German Federal Ministry of Education and Research (BMBF) project MINE of the Geotechnologien Programme (Grant of project BMBF03G0737A).

References

Blanco-Montenegro, I., I. Nicolosi, A. Pignatelli, and M. Chiappini (2008). Magnetic imaging of the feeding system of oceanic volcanic islands: El Hierro (Canary Islands), *Geophys. J. Int.* **173,** 339–350, doi: 10.1111/j.1365-246X.2008.03723.x.

Carracedo, J. C., E. R. Badiola, H. Guillou, J. de la Nuez, and F. J. Pérez Torrado (2001). Geology and volcanology of La Palma and El Hierro, Western Canaries, *Estud. Geol.* **57,** 175–273.

Carracedo, J. C., F. Pérez-Torrado, A. Rodríguez, J. L. Fernández Turiel, A. Klügell, V. R. Troll, and S. Wiesmaier (2012). The ongoing volcanic eruption of El Hierro, Canary Islands, *Eos Trans. AGU* **93,** no. 9, 89–90, doi: 10.1029/2012EO090002.

Carracedo, J. C., E. Rodríguez Badiola, H. Guillou, M. Paterne, S. Scaillet, F. J. Pérez Torrado, R. Paris, U. Fra-Paleo, and A. Hasen (2007). Eruptive and structural history of Teide Volcano and Rift zones of Tenerife, Canary Islands, *Geol. Soc. Am. Bull.* **119,** 1027–1051, doi: 10.1130/B26087.1.

Cesca, S., J. Battaglia, T. Dahm, E. Tessmer, S. Heimann, and P. Okubo (2008). Effects of topography and crustal heterogeneities on the source estimation of LP event at Kilauea volcano, *Geophys. J. Int.* **172,** 1219–1236, doi: 10.1111/j.1365-246X.2007.03695.x.

Cesca, S., E. Buforn, and T. Dahm (2006). Amplitude spectra moment tensor inversion of shallow earthquakes in Spain, *Geophys. J. Int.* **166,** 839–854, doi: 10.1111/j.1365-246X.2006.03073.x.

Cesca, S., S. Heimann, K. Stammler, and T. Dahm (2010). Automated procedure for point and kinematic source inversion at regional distances, *J. Geophys. Res.* **115,** no. B06304, doi: 10.1029/2009JB006450.

Cesca, S., A. Rohr, and T. Dahm (2013). Discrimination of induced seismicity by full moment tensor inversion and decomposition, *J. Seismol.* **17,** 147–163, doi: 10.1007/s10950-012-9305-8.

Dañobeitia, J. J. (1980). Interpretación de la estructura de la corteza en el Archipiélago Canario a partir de perfiles sísmicos profundos de refracción, *Ph.D. Thesis*, Universidad Complutense de Madrid, Madrid, Spain.

Domínguez Cerdeña, I., C. del Fresno, and A. Gomis Moreno (2014). Seismicity patterns prior to the 2011 El Hierro eruption, *Bull. Seismol. Soc. Am.* **104,** 567–575, doi: 10.1785/0120130200.

Domínguez Cerdeña, I., C. del Fresno, and L. Rivera (2011). New insight on the increasing seismicity during Tenerife's 2004 volcanic reactivation, *J. Volcanol. Geoth. Res.* **206,** 15–29, doi: 10.1016/j.jvolgeores.2011.06.005.

Efron, B. (1982). *The Jacknife, the Bootstrap, and Other Resampling Plans*, Society of Industrial and Applied Mathematics, Philadelphia, Pennsylvania, doi: 10.1137/1.9781611970319.fm.

Goldstein, P., and A. Snoke (2005). SAC availability for the IRIS community, *Incorporated Institutions for Seismology Data Management Center*, Electronic Newsletter, available online at http://www.iris.edu/dms/newsletter/vol7/no1/sac-availability-for-the-iris-community/ (last accessed November 2014).

Heimann, S. (2011). A robust method to estimate kinematic earthquake source parameters, *Ph.D. Thesis*, Universität Hamburg, Hamburg, Germany.

Hill, D. P. (1977). A model for earthquake swarms, *J. Geophys. Res.* **82,** 1347–1352, doi: 10.1029/JB082i008p01347.

Ibáñez, J. M., S. De Angelis, A. Díaz-Moreno, P. Hernández, G. Alguacil, A. Posadas, and N. Pérez (2012). Insights into the 2011–2012 submarine eruption off the coast of El Hierro (Canary Islands, Spain) from statistical analyses of earthquake activity, *Geophys. J. Int.* **191,** 659–670, doi: 10.1111/j.1365-246X.2012.05629.x.

Jiménez-Munt, I., M. Fernández, M. Torne, and P. Bird (2001). The transition from linear to diffuse plate boundary in the Azores–Gibraltar region: Results from a thin-sheet model, *Earth Planet. Sci. Lett.* **192,** 175–189, doi: 10.1016/S0012-821X(01)00442-3.

Krieger, L., and S. Heimann (2012). MoPaD—moment tensor plotting and decomposition: A tool for graphical and numerical analysis of seismic moment tensors, *Seismol. Res. Lett.* **83,** 589–595, doi: 10.1785/gssrl.83.3.589.

López, C., M. J. Blanco, R. Abella, B. Brenes, V. M. Cabrera Rodríguez, B. Casas, I. Domínguez Cerdeña, A. Felpeto, M. Fernández de Villalta, C. del Fresno, *et al.* (2012). Monitoring the volcanic unrest of El Hierro (Canary Islands) before the onset of the 2011–2012 submarine eruption, *Geophys. Res. Lett.* **39,** L13303, doi: 10.1029/2012GL051846.

López, C., J. Martí, R. Abella, and M. Tárraga (2014). Applying fractal dimensions and energy-budget analysis to characterize fracturing processes during magma migration and eruption: 2011–2012 El Hierro (Canary Islands) submarine eruption, *Surv. Geophys.* 1–22, doi: 10.1007/s10712-014-9290-2.

Martí, J., V. Pinel, C. López, A. Geyer, R. Abella, M. Tárraga, M. J. Blanco, A. Castro, and C. Rodríguez (2013). Causes and mechanisms of the 2011–2012 El Hierro (Canary Islands) submarine eruption, *J. Geophys. Res.* **118,** 1–17, doi: 10.1002/jgrb.50087.

Meletlidis, S., A. D. Roberto, M. Pompilio, A. Bertagnini, I. Iribarren, A. Felpeto, P. A. Torres, and C. D. Oriano (2012). Xenopumices from the 2011–2012 submarine eruption of El Hierro (Canary Islands, Spain): Constraints on the plumbing system and magma ascent, *Geophys. Res. Lett.* **39,** 1–6, doi: 10.1029/2012GL052675.

Mezcua, J., E. Buforn, A. Udías, and J. Rueda (1992). Seismotectonics of the Canary Islands, *Tectonophysics* **208,** 447–452.

Ranero, C. R., and M. Torne (1995). Gravity and multichannel seismic reflection constraints the lithospheric structure of the Canary swell, *Mar. Geophys. Res.* **17,** no. 3, 519–534, doi: 10.1007/BF01204342.

Roman, D. C., and K. V. Cashman (2006). The origin of volcano-tectonic earthquake swarms, *Geology* **34,** 457–460, doi: 10.1130/G22269.1.

Romanowicz, B. A. (1982). Moment tensor inversion of long period Rayleigh waves: A new approach, *J. Geophys. Res.* **87,** no. B7, 5395–5407, doi: 10.1029/JB087iB07p05395.

Rueda, J., and J. Mezcua (2005). Near-real-time seismic moment-tensor determination in Spain, *Seismol. Res. Lett.* **76,** 455–465.

Sainz-Maza Aparicio, S., J. Arnoso Sampedro, F. González Montesinos, and J. Martí Molist (2014). Volcanic signatures in time gravity variations during the volcanic unrest on El Hierro (Canary Islands), *J. Geophys. Res.* **119,** 5033–5051, doi: 10.1002/2013JB010795.

Shuler, A., M. Nettles, and G. Ekström (2013). Global observation of vertical-CLVD earthquakes at active volcanoes, *J. Geophys. Res.* **118,** 138–164, doi: 10.1029/2012JB009721.

Silva, R., J. Havskov, C. Bean, and N. Wallenstein (2012). Seismic swarms, fault plane solutions, and stress tensors for Sao Miguel Island central region (Azores), *J. Seismol.* **16,** 389–407, doi: 10.1007/s10950-012-9275-x.

Snoke, J. A., J. W. Munsey, A. C. Teague, and G. A. Bollinger (1984). A program for focal mechanism determination by combined use of polarity and *SV–P* amplitude ratio data, *Earthq. Notes* **55,** no. 3, 15.

Stroncik, N., A. Klügel, and T. Hansteen (2009). The magmatic plumbing system beneath El Hierro (Canary Islands): Constraints from phenocrysts and naturally quenched basaltic glasses in submarine rocks, *Contrib. Mineral. Petrol.* **157,** 593–607, doi: 10.1007/s00410-008-0354-5.

Udías, A., and E. Buforn (1988). Single and joint fault plane solutions from first motion data, in *Seismological Algorithms*, D. Doorbons (Editor), Academic Press, London, United Kingdom, 443–453.

Ukawa, M., and H. Tsukahara (1996). Earthquake swarms and dike intrusions off the east coast of Izu Peninsula, central Japan, *Tectonophysics* **253,** 285–303, doi: 10.1016/0040-1951(95)00077-1.

Umakoshi, K., N. Itasaka, and H. Shimizu (2011). High-frequency earthquake swarm associated with the May 1991 dome extrusion at Unzen Volcano, Japan, *J. Volcanol. Geoth. Res.* **206,** 70–79, doi: 10.1016/j.jvolgeores.2011.07.004.

Waldhauser, F., and W. L. Ellsworth (2000). A double-difference earthquake location algorithm: Method and application to the northern Hayward fault, California, *Bull. Seismol. Soc. Am.* **90,** 1353–1368, doi: 10.1785/0120000006.

Watts, A. B. (1994). Crustal structure, gravity-anomalies and flexure of the lithosphere in the vicinity of the Canary-islands, *Geophys. J. Int.* **119,** 648–666, doi: 10.1111/j.1365-246X.1994.tb00147.x.

Wessel, P., and W. H. F. Smith (1998). New, improved version of generic mapping tools released, *Eos Trans. AGU* **79,** 579–579, doi: 10.1029/98EO00426.

Observatorio Geofísico Central
Instituto Geográfico Nacional (IGN)
c/ Alfonso XII, 3
28014 Madrid, Spain
cdelfresno@fomento.es
(C.d.F.)

Centro Geofísicon de Canarias
Instituto Geográfico Nacional (IGN)
c/La Marina 20. 2°
38001 S/C de Tenerife, Spain
(I.D.C.)

GFZ German Research Centre for Geosciences
Telegrafenberg
14473 Potsdam, Germany
(S.C.)

Dpto. Física de la Tierra I (Geofísica y Meteorología)
Facultad de Ciencias Físicas
Universidad Complutense de Madrid
Ciudad Universitaria s/n
28040 Madrid, Spain
(E.B.)

Manuscript received 4 June 2014;
Published Online 9 December 2014